# Quantum dynamical investigation of the simplest Criegee intermediate CH2OO and its O–O photodissociation channels

Kousik Samanta, Joseph M. Beames, Marsha I. Lester, and Joseph E. Subotnik

Citation: The Journal of Chemical Physics **141**, 134303 (2014); doi: 10.1063/1.4894746
View online: http://dx.doi.org/10.1063/1.4894746
View Table of Contents: http://scitation.aip.org/content/aip/journal/jcp/141/13?ver=pdfcov
Published by the AIP Publishing

# Quantum dynamical investigation of the simplest Criegee intermediate $CH_2OO$ and its O–O photodissociation channels

Kousik Samanta,[a] Joseph M. Beames, Marsha I. Lester,[b] and Joseph E. Subotnik[b]
*Department of Chemistry, University of Pennsylvania, Philadelphia, Pennsylvania 19104-6323, USA*

(Received 14 June 2014; accepted 25 August 2014; published online 2 October 2014)

The singlet electronic potential energy surfaces for the simplest Criegee intermediate $CH_2OO$ are computed over a two-dimensional reduced subspace of coordinates, and utilized to simulate the photo-initiated dynamics on the $S_2$ ($B$) state leading to dissociation on multiple coupled excited electronic states. The adiabatic electronic potentials are evaluated using dynamically weighted state-averaged complete active space self-consistent field theory. Quasi-diabatic states are constructed from the adiabatic states by maximizing the charge separation between the states. The dissociation dynamics are then simulated on the diabatically coupled excited electronic states. The $B \leftarrow X$ electronic transition with large oscillator strength was used to initiate dynamics on the $S_2$ ($B$) excited singlet state. Diabatic coupling of the $B$ state with other dissociative singlet states results in about 5% of the population evolving to the lowest spin-allowed asymptote, generating $H_2CO$ ($X\,^1A_1$) and O ($^1$D) fragments. The remaining ∼95% of the population remains on repulsive $B$ state and dissociates to $H_2CO$ ($a\,^3A''$) and O ($^3$P) products associated with a higher asymptotic limit. Due to the dissociative nature of the $B$ state, the simulated electronic absorption spectrum is found to be broad and devoid of any vibrational structure. © *2014 AIP Publishing LLC*. [http://dx.doi.org/10.1063/1.4894746]

## I. INTRODUCTION

Ozonolysis of alkenes plays a very important role in troposphere chemistry, oxidizing alkenes produced both anthropogenically and biogenically.[1–5] The reaction mechanism for ozonolysis proceeds through addition of ozone to an alkene double bond, forming a primary ozonide with sufficient energy to undergo further unimolecular decay to produce a carbonyl species and a carbonyl oxide, known as a Criegee intermediate. The Criegee intermediate is itself formed with a high degree of internal excitation, and can undergo unimolecular decay to various small molecular species such as OH, $HO_2$, CO, $CO_2$, and $CH_3$.

The production of Criegee intermediates by ozonolysis has been proposed for a long time, but only recently has even the simplest Criegee intermediate $CH_2OO$ been detected directly, partly as a result of a new method for generating the intermediates in the laboratory.[6] Many of the recent studies focus on bimolecular reactions of $CH_2OO$ with key atmospheric constituents such as $NO_2$, $SO_2$ and $H_2O$.[7] Beames *et al.*[8] also identified a broad absorption for $CH_2OO$ in the near UV, peaked at 335 nm, with a large peak absorption cross section (on the order of $5 \times 10^{-17}$ cm$^2$ molecule$^{-1}$). The $CH_2OO$ UV absorption spectrum was observed as a very significant depletion of the associated vacuum ultraviolet (VUV) photoionization signal and by other absorption methods.[9,10] $CH_2OO$ absorption leads to rapid cleavage of the O–O bond, resulting in the production of atomic oxygen fragments. Two spin-allowed asymptotic limits are energetically accessible: the lowest $H_2CO$ ($X\,^1A_1$) + O ($^1D$) limit and a higher $H_2CO$ ($a\,^3A''$) + O ($^3P$) limit. The velocity and angular distributions of the O ($^1$D) fragments have been reported recently,[11] while analogous experiments on the O ($^3P$) fragments, motivated by the present study, will be presented in Ref. 12.

Early electronic structure calculations on the simplest Criegee intermediate created a degree of controversy over the nature of the bonding at the equilibrium geometry in the ground electronic state. $CH_2OO$ is isoelectronic with ozone, and suffers the same challenges to electronic structure theory of having mixed biradical/zwitterionic character.[13,14] The mixture of electronic character must be treated correctly to represent the optimized geometry and energy of the system at different nuclear geometries. In particular the relative electronic character of the system is directly evident in the C–O and O–O bond lengths: a purely biradical depiction of the system distributes the $\pi$ electron density evenly over the C–O–O group giving rise to similar C–O/O–O bond lengths. In contrast, predominantly zwitterionic character shortens the C–O bond, making it similar to a C=O double bond.

From a computational point of view, Hartree-Fock (HF) theory gives a zwitterionic description of the carbonyl oxide moiety, while second order post-HF perturbative corrections (for example, MP2) give a much more biradical picture of the bonding.[15,16] Bartlett and co-workers have shown that including higher order perturbation theory beyond second order leads to oscillating results between zwitterionic and biradical character that have not converged at MP4; instead Bartlett and co-workers highlight coupled cluster results which are significantly more zwitterionic in nature than MP2.[16,17]

Multireference methods should ideally provide a better description of the system. The desire to treat the ground state

[a] Present address: School of Basic Sciences, Indian Institute of Technology, Bhubaneswar, Odisha 751007, India.
[b] Authors to whom correspondence should be addressed. Electronic addresses: milester@sas.upenn.edu and subotnik@sas.upenn.edu.

 

of carbonyl oxides in a multireference fashion can be drawn from a physical picture of several resonance structures contributing to the ground state wavefunction, thus creating the need for some treatment of static electron correlation.[18–22] Illustrations of this can be found in the works of Nguyen *et al.*[20] and Kalinowski *et al.*[23] where the main configuration interaction (CI) vectors contributing to the ground state wavefunction are explicitly displayed. These vectors indicate that the predominant electronic configurations that contribute to the ground state wavefunction are zwitterionic in nature, suggesting that Criegee intermediates are predominantly zwitterionic in character. Most multireference methods produce optimized geometries for $CH_2OO$ that are very similar to one another. Interestingly, these geometries can be relatively well reproduced by both coupled cluster calculations with single, double and perturbative triple excitations (CCSD(T)) and density functional theory calculations.[16,17,24–27] Experimental determinations of the structure of $CH_2OO$ have now been achieved based on microwave rotational constants and infrared vibrational frequencies derived from Fourier transform microwave (FTMW) and Fourier transform infrared (FTIR) experiments, and compared with high level *ab initio* calculations using both CCSD(T) and CASSCF with *n*-electron valence state perturbation theory (CASSCF/NEVPT2) methods.[26,28–30] The experimental geometries show a significant shortening of the C–O bond with respect to a typical single bond, suggesting a more zwitterionic bonding character, which is consistent with the theoretical consensus outlined above.

The present article focuses on the photodissociation dynamics of the Criegee intermediate $CH_2OO$, which requires computing several singlet electronic potential energy surfaces for the system. Until this point, there has been little theoretical work investigating the excited electronic states of Criegee intermediates. Theoretical examination of the electronic states for the smallest Criegee intermediate began with the use of $\pi$POL(2)CI method, which predicts an optically bright $\pi^*$-$\pi$ transition at ~3.66 eV with a significant oscillator strength ($f \sim 0.1$).[15] This predicted absorption was described as analogous to the Hartley band of ozone. These calculations compare very favorably with the recently measured absorption spectrum for $CH_2OO$ in both peak position and cross section. In the 1980s and early 1990s complete neglect of differential overlap for spectroscopy (CNDO/S) calculations were used to predict the excitation energies for larger conjugated Criegee intermediates (thought to have been isolated in matrices) and as a tool to examine the effects of substitution on the UV spectra.[24,31] More recent work by Lee *et al.*[27] examined the vertical excitation energy of the smallest Criegee intermediate from its ground $X\,^1A'$ to the $B\,^1A'$ state which corresponds to the $\pi^*$-$\pi$ transition identified in the earlier work. Lee *et al.*[27] used various methods to optimize both ground and excited state geometries and subsequently investigate how Franck-Condon factors may influence the absorption spectrum, but this study did not investigate the shape and couplings between the upper potential energy surfaces. These couplings are crucial in understanding the spectroscopy and photodissociation dynamics of $CH_2OO$.

Let us now turn our attention to prior theoretical studies of $CH_2OO$ photodissociation. The adiabatic potential energy surfaces produced in the CASSCF with second order Rayleigh-Schrödinger perturbation theory (CASPT2) work of Aplincourt *et al.*[18] showed that the adiabatic *B* state is repulsive in the O–O coordinate and provided the first theoretical prediction of the photodissociation process later observed experimentally. Similar CASSCF calculations were later carried out by Beames *et al.*[8] to generate the repulsive adiabat accessed from the ground state in the Franck-Condon region. These potentials were used to model the UV absorption of $CH_2OO$ as a broad unstructured spectrum, in good accord with the experimental data, based on the classical reflection principle approximation in one dimension (the O–O dissociation coordinate). Later, the excited state potential energy surfaces were estimated using equations-of-motion coupled cluster calculations (EOM-CCSD) for both $CH_2OO$ and $CH_3CHOO$.[32] These surfaces indicate that the photo-initiated dynamics are likely to be very similar for $CH_2OO$ and many alkyl-substituted Criegee intermediates generated by alkene ozonolysis in the troposphere.

The goal of the present theoretical study is to investigate the photodissociation dynamics of $CH_2OO$ with the intention to connect with recent experimental studies and make reasonable predictions of additional observables. To do so, we require potential energy surfaces and couplings from the Franck-Condon region to the dissociation limit. For such a goal we are prepared to sacrifice some spectroscopic accuracy (more accurate calculations can routinely be performed in the Franck-Condon region alone). The adiabatic potential energy surfaces for $CH_2OO$ will be initially computed on a two-dimensional grid defined along the O–O bond length and C–O–O bond angle. Localized diabatic states are then constructed. Finally, the diabatic surfaces and wavepacket dynamics on these surfaces are utilized to model various experimental observables arising from electronic excitation of $CH_2OO$ on the strong $B \leftarrow X$ transition.

## II. METHODS

### A. *Ab initio* adiabatic potential energy surfaces

We used dynamically weighted state-averaged CASSCF (DW-SA-CASSCF) method to optimize the ground state geometry as well as to compute the adiabatic potential energy surfaces of the simplest Criegee intermediate, $CH_2OO$. A brief description of the notation used throughout the text is summarized in Table I.

The DW-SA-CASSCF requires variational minimization of the dynamically weighted energy functional for the desired state (here, the ground state):

$$E = \sum_J E_J \, W(E_J - E_0), \tag{1}$$

where $W(x) = \mathrm{sech}^2(-x/\beta)$.[33] The CASSCF method generates accurate multi-reference wavefunctions by simultaneously optimizing orbitals and configurations. State-averaging should ensure that the optimized orbitals give a good description of the ground *as well as* the excited states.[34] It also orthonormalizes the computed CASSCF states and allows us to compute matrix elements involving two different states (e.g.,

TABLE I. Description of frequently used notations and symbols in this article.

| Indices and constants | | Operators, matrices and vectors | |
|---|---|---|---|
| $p, q$ | nuclear grid | $\hat{H}$ | total Hamiltonian |
| $J, K$ | adiabats | $\hat{H}_{\text{el}}$ | electronic Hamiltonian |
| $A, B$ | diabats | $\hat{T}_{\text{nuc}}$ | nuclear kinetic energy operator |
| $n$ | vibronic state index | $\hat{\boldsymbol{\mu}}$ | dipole operator |
| $n'$ | vibronic state index corresponding to coupled diabats only | $\mathbf{H}$ | $\hat{H}$ in the $\{\|\mathbf{R}_p\rangle\} \otimes \{\|\Xi_A\rangle\}$ basis |
| $N_{\text{states}}$ | number of states diabatized | $[\mathbf{H}_{AB}]$ | $N_{\text{grids}} \times N_{\text{grids}}$ submatrix of $\mathbf{H}$ |
| $N_{\text{grids}}$ | total number of nuclear grid points | $\mathbf{V}$ | $\hat{H}_{\text{el}}$ in diabatic basis |
| $\beta$ | parameter for dynamic CASSCF state weighting | $\mathbf{T}$ | nuclear kinetic energy matrix |
| Functions | | $\boldsymbol{\mu}$ | dipole moment matrix |
| | | $\varepsilon_n$ | vibronic energy |
| $\|\Phi_J\rangle$ | adiabatic state | $\mathbf{r}$ | electronic coordinates |
| $\|\Xi_A\rangle$ | diabatic state | $\mathbf{R}$ | nuclear coordinates |
| $\|\Psi_n\rangle$ | vibronic state | $\mathbf{R}_p$ | a nuclear grid point |
| $\|\chi_n^A\rangle$ | nuclear counterparts of $\|\Xi_A\rangle$ in $\|\Psi_n\rangle$ | $\mathbf{d}$ | derivative coupling |
| $\|\tilde{\Psi}(t)\rangle$ | excited wavepacket at time $t$ | $\mathbf{U}$ | adiabatic-to-diabatic transformation |
| $\|\xi_A\rangle$ | projection of a wavepacket on $\|\Xi_A\rangle$ | $C_n^{A,p}$ | projection of $\|\chi_n^A\rangle$ on $\|\mathbf{R}_p\rangle$ |
| $\|\mathbf{R}_p\rangle$ | nuclear grid basis function localized at $\mathbf{R}_p$ | $\zeta_n$ | projection of a wavepacket on $\|\Psi_n\rangle$ |
| $S_A$ | diabatic surface / state | | |

transition dipole moment). Dynamic weighting helps make the potential energy surfaces smooth for dynamical studies, and prevent random intrusion of higher states. In this study, the lowest eight CASSCF states were dynamically weighted with an energy parameter $\beta = 2$ eV. In general, for an optical assessment of excited state energies, one would prefer a large $\beta$ value (or perhaps simply equal state weightings). That being said, we require smooth potential energy surfaces for excited state wavepacket dynamics, therefore, we find $\beta = 2$ eV to be a reasonable compromise between "accurate" state energies and smooth surfaces. All the electronic structure calculations were performed using GAMESS suite of computer programs.[35,36]

Within the context of CASSCF, a careful choice of the active space should account for most electron correlation in such a small molecule. In practice, given the necessary balance between zwitterionic and biradical configurations, we expect the amount of static correlation to be larger than dynamic correlation. Our active space consisted of 10 orbitals with 14 electrons. These orbitals included all the valence orbitals ($2s$ and $2p$) of C and O except for those involved in C–H bonding. We chose these orbitals because we are interested in the stretching and bending of the C–O–O framework.

For each C and O atom, a modified version of aug-cc-pVTZ basis set[37] was used where the *f* functions were deleted from the standard set and two additional sets of Rydberg basis functions[38] were included. The standard cc-pVDZ basis set[37] was used for all the H atoms. In total, our basis set consisted of 160 spherical basis functions.

A few words are now in order about our choice of nuclear geometries. In all calculations below, we have settled on a simple two-dimensional reduced coordinate subspace where all internal degrees of freedom are frozen except for the $R_{O_1O_2}$ distance and the $a_{CO_1O_2}$ angle. Of course, ideally, one would construct full dimensional potential energy surfaces over which one could run exact quantum dynamics simulations. Unfortunately, with 9 internal degrees of freedom, such a lofty goal was beyond the scope of this work. Our rationale for picking a reduced space of $R_{O_1O_2}$ and $a_{CO_1O_2}$ was as follows: First, Beames *et al.*[8,32] have shown previously that a conical intersection can be expected in the excited state manifold of $CH_2OO$. As such, in order to capture a slice of the two-dimensional branching space and represent nuclear dynamics around a conical section, we require a minimum of two nuclear coordinates. Second, in our own preliminary calculations, we observed that three obvious internal coordinates had non-zero projections on the derivative couplings between the second and fourth adiabatic states, namely, $R_{O_1O_2}$, $a_{CO_1O_2}$, and $R_{O_1C}$. In principle, we would have preferred to generate all potential energy surfaces over a three-dimensional grid spanned by these internal coordinates. In practice, however, we found that constructing smooth diabatic states was not possible over this three-dimensional space; the problem becomes that there is no well-defined small energetic window which contains a fixed number of states of the same character. As such, no global diabatization appears to be possible. As a result, we settled on the two-dimensional space ($R_{O_1O_2}$, $a_{CO_1O_2}$). Future work will no doubt explore the ramifications of including $R_{O_1C}$ in the quantum dynamics and spectroscopy of $CH_2OO$.

This study focuses on the low-lying singlet states of the simplest Criegee intermediate, $CH_2OO$, and in particular the $B \leftarrow X$ transition, which is responsible for a broad absorption spectrum.[8] The singlet ground state was found to be well-separated from the excited singlet states energetically, except at very large $R_{O_1O_2}$. However, the present study shows that several excited states come close together for the geometries in the vicinity of the Franck-Condon region. Thus, in order to obtain smooth diabatic states (see below), it was necessary to start with a basis of seven excited states. Below, after diabatization, these state are denoted as $S_1 - S_7$. Since we were averaging over eight singlet states, we had to compute a large

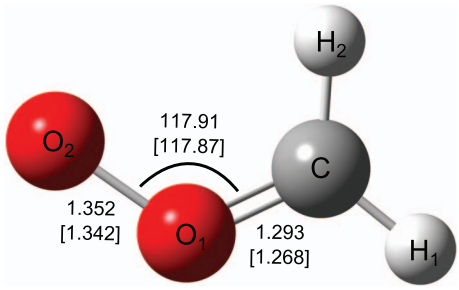


FIG. 1. Geometric structure of the smallest Criegee intermediate $CH_2OO$. Three key calculated parameters are shown: $R_{O_1O_2}$ (Å), $R_{O_1C}$ (Å), and $a_{CO_1O_2}$ (°). These values are taken from the DW-SA-CASSCF $S_0$ minimum energy structure computed in this work. Values in brackets are derived from experiment,[29] and are shown for comparison.

number of CASSCF states in order to find the states with the correct spin symmetry — sometimes as many as 25 (including triplets, quintets, etc.). The higher lying states are often very diffuse, and to correctly describe them one needs Rydberg type diffuse functions in the basis set.

Two-dimensional adiabatic potential energy surfaces were constructed by evaluating DW-SA-CASSCF energies on a uniform two-dimensional grid of points along the $O_1$–$O_2$ bond distance ($R_{O_1O_2}$) from 1.00 Å to 3.00 Å at every 0.02 Å interval[39] and the C–$O_1$–$O_2$ bond angle ($a_{CO_1O_2}$) from 80° to 160° at every 10° interval. All the other geometric parameters were kept fixed at their ground state equilibrium values. Numbering of atomic centers are displayed in Fig. 1. All calculations were performed without symmetry restrictions despite the $C_s$ ground state minimum energy structure. No attempt has been made to ascribe the symmetry of the ground or excited electronic states, although symmetry labels have been used to label the asymptotic limits of the computed surfaces.

### B. Diabatization

Diabatic states $\{|\Xi_A\rangle\}$ are formally defined[40] as those states for which all the derivative coupling elements $\mathbf{d}_{AB}$ are zero:

$$\mathbf{d}_{AB} = \langle \Xi_A | \nabla_{\mathbf{R}} | \Xi_B \rangle_{\mathbf{r}} = \mathbf{0}. \tag{2}$$

Here $\mathbf{R}$ and $\mathbf{r}$ represent nuclear and electronic coordinates, respectively, $\nabla_{\mathbf{R}}$ is the gradient operator in terms of the nuclear coordinates, and $\langle ... \rangle_{\mathbf{r}}$ indicates integration over electronic coordinates only.

One can attempt to construct diabatic states from a basis of $N_{\text{states}}$ adiabatic states $\{|\Psi_J\rangle\}$

$$|\Xi_A(\mathbf{r};\mathbf{R})\rangle = \sum_{J=1}^{N_{\text{states}}} |\Psi_J(\mathbf{r};\mathbf{R})\rangle \, U_{JA} \tag{3}$$

using an adiabatic-to-diabatic transformation $\mathbf{U}$. However, for finite $N_{\text{states}}$, no solution $\mathbf{U}$ exists such that all $\mathbf{d}_{AB}$ in the diabatic basis is zero.[41] That being said, the quasi-diabatic states (for which $\mathbf{d}_{AB}$s are very small) are often good enough for dynamics. From now on, we shall refer to the quasi-diabatic states as *diabats* when there is no chance of ambiguity and the adiabatic states as *adiabats*. Since there is no unique $\mathbf{U}$, there are several methods of constructing quasi-diabatic states,[42] often based on a physical observable. The dipole moment has a long history in such context.[43–48] In this work, we obtained $\mathbf{U}$ for each nuclear geometry by maximizing

$$p(\mathbf{U}) = \sum_{J,K=1}^{N_{\text{states}}} |\tilde{\boldsymbol{\mu}}_{JJ} - \tilde{\boldsymbol{\mu}}_{KK}|^2, \tag{4}$$

where

$$\tilde{\boldsymbol{\mu}}_{JK} = \begin{cases} \boldsymbol{\mu}_{JK} & \text{if } J = K \\ \boldsymbol{\mu}_{JK}\,\lambda_J\,\lambda_K & \text{if } J \neq K, \end{cases} \tag{5}$$

$$\boldsymbol{\mu}_{JK} = \langle \Phi_J | \hat{\boldsymbol{\mu}} | \Phi_K \rangle. \tag{6}$$

Here, $\hat{\boldsymbol{\mu}}$ is the dipole operator and $\lambda_J$ is a damping factor based on the energy of the $J$th adiabat (see below). If we set $\lambda_J = 1$ for all $J$, then the diabatization method is known as Boys localization[49] (and generalized Mulliken-Hush in one dimension),[43,44] where the diabats are constructed by maximizing the charge separation [see Ref. 45 for details]. For $N_{\text{states}} = 2$, there is an exact analytical solution for $\mathbf{U}$:

$$\mathbf{U} = \begin{pmatrix} \cos\theta & \sin\theta \\ -\sin\theta & \cos\theta \end{pmatrix}, \tag{7}$$

where

$$\theta = \frac{1}{4}\tan^{-1}\left(\frac{G}{-F}\right), \tag{8}$$

$$F = \left|\boldsymbol{\mu}_{12}^0\right|^2 - \left|\boldsymbol{\mu}_{11}^0 - \boldsymbol{\mu}_{22}^0\right|^2/4, \tag{9}$$

$$G = \boldsymbol{\mu}_{12}^0 \cdot \left(\boldsymbol{\mu}_{11}^0 - \boldsymbol{\mu}_{22}^0\right), \tag{10}$$

$$\boldsymbol{\mu}_{JK}^0 = \langle \Phi_J | \hat{\boldsymbol{\mu}} | \Phi_K \rangle. \tag{11}$$

For $N_{\text{states}} > 2$, $p(\mathbf{U})$ is maximized by rotating together all the relevant electronic states in pairs in a self-consistent fashion.[49] Thus, this method requires only the dipole moment elements and there is no need to compute computationally demanding $\mathbf{d}$. Recent work has shown that derivative couplings between the Boys localized diabats can indeed be very small.[48,50]

Now we turn to discuss damping based on the energy criterion. For $CH_2OO$, we diabatized the seven lowest singlet states, among which there were crossings in the regions of the potential energy surfaces pertinent to the previously experimentally observed spectra and UV-induced photodissociation dynamics. However, at some geometries the higher-lying states cannot be diabatized reliably since there are crossings with even higher states not included in the adiabatic basis. Given our interest in only the states below a threshold of energy ($E_{\text{thresh}}$), and at the same time, the need for smooth diabats for the dynamics study, we rescaled the off-diagonal dipole moment matrix elements ($\boldsymbol{\mu}_{JK}$, $J \neq K$) with $\lambda_J\lambda_K$ [see Eq. (5)], where

$$\lambda_J = \frac{1}{2}\,\text{erfc}\left(\frac{E_J - E_{\text{thresh}}}{\alpha}\right), \tag{12}$$

$\alpha = 5.0 \times 10^{-3}$ hartree, $E_J$ is the energy of the $J$th adiabat, and $E_{\text{thresh}} = -188.535$ hartree. $E_{\text{thresh}}$ is $50.4 \times 10^3$ cm$^{-1}$ above the ground state minimum. The parameter $\alpha$ was chosen as a compromise between a value small enough that we could ignore very high energy electronic states ($\lambda_J$ would resemble a step function) and a value large enough so that smooth potential energies would be retained. In this work, the rescaled dipole moment ($\tilde{\boldsymbol{\mu}}$) was used only to compute $\mathbf{U}$ and define the diabats; for all other applications we used the original dipole moments $\boldsymbol{\mu}$.

Note that Boys localization assumes that the nuclear coordinates trap the system in a metastable state in which electronic transitions are slow compared to nuclear motion. Mathematically, Boys localization can be justified only for the case where the nuclear reorganization energy is larger than the diabatic coupling between electronic states. For the case of two or more electronic states with the same charge centers, electronic transitions can be fast compared to nuclear motion and diabatic couplings can be larger than reorganization energies. To overcome the problem, as suggested by Cave and Newton,[43,44] the simplest solution is to block-diagonalize the electronic Hamiltonian ($\hat{H}_{\text{el}}$) in the basis of the localized diabats:

$$V_{AB}(\mathbf{R}) = \langle \Xi_A(\mathbf{r};\mathbf{R})|\hat{H}_{\text{el}}|\Xi_B(\mathbf{r};\mathbf{R})\rangle_{\mathbf{r}}, \tag{13}$$

where each block includes all the diabats with charge localized on the same charge center. In the case of $CH_2OO$, we note that all electronic states can be divided into two groups: those with charge transfer character and those without charge transfer character relative to the ground state, i.e., those with "mostly zwitterionic" character or "mostly biradical" character. We diagonalize the Hamiltonian within each of these groups. In so doing, we isolate the couplings only between those electronic states with different charge centers. In what follows, the diabats $\{|\Xi_A\rangle\}$ refer to those quasi-diabatic states in terms of which $V_{AB} = 0$ when $|\Xi_A\rangle$ and $|\Xi_B\rangle$ have similar charge distributions but $V_{AB} \neq 0$ if $|\Xi_A\rangle$ and $|\Xi_B\rangle$ have different charge distributions. The phase of the diabats were chosen such that the transition dipole matrix elements in the diabatic basis vary smoothly from one grid point to the next.

### C. Vibronic states

Now we turn to the evaluation of the vibronic wavefunctions, $\{\Psi_n(\mathbf{r},\mathbf{R})\}$, which are necessary for quantum dynamical calculations as well as simulating electronic spectra. $|\Psi_n\rangle$ satisfies the Schrödinger equation

$$\hat{H}|\Psi_n\rangle = \varepsilon_n|\Psi_n\rangle, \tag{14}$$

where $\hat{H}$ is the full Hamiltonian and $\varepsilon_n$ is the corresponding eigenvalue. Using a Born-Huang type expansion,[51] we can express $|\Psi_n\rangle$ in terms of the diabats[52] as

$$\Psi_n(\mathbf{r},\mathbf{R}) = \sum_A \chi_n^A(\mathbf{R})\ \Xi_A(\mathbf{r}), \tag{15}$$

$$|\Psi_n\rangle = \sum_A \sum_{p=1}^{N_{\text{grids}}} C_n^{A,p}\ |\mathbf{R}_p\rangle\ |\Xi_A\rangle, \tag{16}$$

where $|\chi_n^A\rangle$ is the nuclear part of the vibronic wavefunction, $C_n^{A,p} = \langle \mathbf{R}_p|\chi_n^A\rangle$ is the expansion coefficient in terms of the nuclear grid basis $\{|\mathbf{R}_p\rangle\}$, $|\mathbf{R}_p\rangle$ is a nuclear grid basis function strongly localized about grid point $\mathbf{R}_p$, and $N_{\text{grids}}$ is the total number of nuclear grid points. The coefficients $\{C_n^{A,p}\}$ completely determine the vibronic wavefunctions for given sets of nuclear grid points and diabats.

Writing $\hat{H}$ in the basis of $\{|\mathbf{R}_p\rangle\} \otimes \{|\Xi_A\rangle\}$ and solving the eigenvalue equation

$$\mathbf{H}\,\mathbf{C}_n = \varepsilon_n\,\mathbf{C}_n, \tag{17}$$

one computes the eigenvector $\mathbf{C}_n$, which has length $N_{\text{states}} \times N_{\text{grids}}$ and whose elements are $C_n^{A,p}$. The explicit form of the Hamiltonian in the $\{|\mathbf{R}_p\rangle\} \otimes \{|\Xi_A\rangle\}$ basis is as follows:

$$[\mathbf{H}_{AB}]_{pq} = \delta_{AB}\ T_{pq} + \delta_{pq}\ V_{AB}(\mathbf{R}_p), \tag{18}$$

where

$$T_{pq} = \langle \mathbf{R}_p|\hat{T}_{\text{nuc}}|\mathbf{R}_q\rangle \tag{19}$$

and $\hat{T}_{\text{nuc}}$ is the nuclear kinetic energy operator. $\mathbf{V}$ is computed by transforming the adiabatic energies obtained from the electronic structure calculations into the diabatic basis [see Sec. II B]. $\mathbf{T}$ is computed in terms of internal coordinates following the discrete variable representation (DVR) approach outlined in Refs. 53 and 54. We constructed $\mathbf{T}$, allowing nuclear motions along the internal coordinates, $R_{O_1O_2}$, $R_{O_1C}$, and $a_{CO_1O_2}$ only. This construction is based on a simplified model—a triatomic M–O–O system—where the pseudo-atom M stands for the $CH_2$ unit and has the same mass as $CH_2$.

Since the ground adiabat ($|\Phi_0\rangle \equiv |\Xi_0\rangle$) was not included in the diabatization of adiabats $|\Phi_1\rangle$–$|\Phi_7\rangle$ [see Sec. II B], the Hamiltonian has a blocked structure

$$\mathbf{H} = \begin{pmatrix} [\mathbf{H}_{00}] & [\,\mathbf{0}\,] & [\,\mathbf{0}\,] & \cdots & [\,\mathbf{0}\,] \\ [\,\mathbf{0}\,] & [\mathbf{H}_{11}] & [\mathbf{H}_{12}] & \cdots & [\mathbf{H}_{17}] \\ [\,\mathbf{0}\,] & [\mathbf{H}_{21}] & [\mathbf{H}_{22}] & \cdots & [\mathbf{H}_{27}] \\ \vdots & \vdots & \vdots & \ddots & \vdots \\ [\,\mathbf{0}\,] & [\mathbf{H}_{71}] & [\mathbf{H}_{72}] & \cdots & [\mathbf{H}_{77}] \end{pmatrix}, \tag{20}$$

where $[\,\mathbf{0}\,]$ is a $N_{\text{grids}} \times N_{\text{grids}}$ matrix of zeros. Consequently, a vibronic wavefunction corresponding to $[\mathbf{H}_{00}]$ block has a very simple form:

$$|\Psi_n\rangle = |\chi_n^0\rangle\,|\Xi_0\rangle. \tag{21}$$

A vibronic wavefunction corresponding to the block of excited states (i.e., the block consisting of submatrices $[\mathbf{H}_{AB}]$ where $1 \le A \le 7$ and $1 \le B \le 7$)

$$|\Psi_{n'}\rangle = \sum_{A=1}^{7} \left|\chi_{n'}^A\right\rangle |\Xi_A\rangle \tag{22}$$

does not include any contribution from $|\Xi_0\rangle$. Here and in what follows, $n'$ refers to vibronic wavefunctions with electronic populations restricted exclusively to the block of excited states (i.e., without a ground state component).

### D. Dynamics in the excited state

The $S_2$ state (the $B$ state) is the optically bright state since the $S_2 \leftarrow S_0$ (i.e., $B \leftarrow X$) transition has the largest oscillator strength in the UV region and is attributed to the broad UV absorption observed experimentally.[8–10] To study the dissociation dynamics of $CH_2OO$ and compute product branching ratios, the ground vibronic state $|\Psi_0\rangle$ was excited to the $S_2$ surface and the ensuing dynamics was simulated over the coupled excited state surfaces.

The excited wavefunction at time $t = 0$,

$$|\tilde{\Psi}(0)\rangle = N\,\hat{\boldsymbol{\mu}}_{02}\,|\Psi_0\rangle = \left|\tilde{\chi}_0^2\right\rangle|\Xi_2\rangle, \tag{23}$$

can be expressed in terms of the vibronic wavefunctions $\{|\Psi_{n'}\rangle\}$ corresponding to the coupling block of $\mathbf{H}$ as

$$|\tilde{\Psi}(0)\rangle = \sum_{n'} \zeta_{n'}\,|\Psi_{n'}\rangle. \tag{24}$$

Here, $N$ is the normalization constant, $|\tilde{\chi}_0^2\rangle = N\sum_p \mu_{02}(\mathbf{R}_p)\,C_0^{0,p}\,|\mathbf{R}_p\rangle$, and $\mu_{02}$ is the projection of the transition moment $\boldsymbol{\mu}_{02}$ in the direction of the polarization of the electromagnetic radiation; we assume $\vec{E}$ is parallel to $\boldsymbol{\mu}_{02}$. We define $\zeta_{n'} = \langle\Psi_{n'}|\tilde{\Psi}(0)\rangle$. The excited wavefunction at time $t$ is given in terms of the time-dependent Schrödinger equation as

$$\begin{aligned}|\tilde{\Psi}(t)\rangle &= e^{-i\hat{H}t/\hbar}\,|\tilde{\Psi}(0)\rangle \\ &= \sum_{n'} \zeta_{n'}\,e^{-i\varepsilon_{n'}t/\hbar}\,|\Psi_{n'}\rangle.\end{aligned} \tag{25}$$

The portion of the wavepacket on diabat $|\Xi_A\rangle$,

$$|\xi_A(t)\rangle = \langle\Xi_A|\tilde{\Psi}(t)\rangle \tag{26}$$

and the corresponding population,

$$P_A(t) = \langle\xi_A(t)|\xi_A(t)\rangle \tag{27}$$

can be used to monitor the propagation of the wavepacket on the diabatic surface $S_A$.

The auto-correlation function $\langle\tilde{\Psi}(0)|\tilde{\Psi}(t)\rangle$ for the excited wavepacket is related to the absorption cross section as[55]

$$\sigma(\omega) \propto \omega\int_{-\infty}^{\infty}\langle\tilde{\Psi}(0)|\tilde{\Psi}(t)\rangle\,e^{i(\varepsilon_0+\hbar\omega)t/\hbar}\,dt \tag{28}$$

$$= \omega\sum_{n'}|\zeta_{n'}|^2\int_{-\infty}^{\infty}e^{-i(\varepsilon_{n'}-\varepsilon_0-\hbar\omega)t/\hbar}\,dt, \tag{29}$$

where $\hbar\omega$ is the energy of an incident photon. In Eq. (29), we assumed the temperature to be 0 K so that initially only the ground vibrational state ($|\Psi_0\rangle$) is occupied. When evaluated within the limit $(-\infty, +\infty)$, the integral on the right reduces to a delta function. However, in practice, we must choose a finite limit (say, $t_{\max}$) which is the time that the wavepacket takes to hit a grid boundary. Thus, we arrive at the following simplified form of the absorption cross section:

$$\begin{aligned}\sigma(\omega) &\propto \omega\sum_{n'}|\zeta_{n'}|^2\int_0^{t_{\max}}\cos[(\varepsilon_{n'}-\varepsilon_0-\hbar\omega)t/\hbar]dt \\ &= \omega\sum_{n'}|\zeta_{n'}|^2\,\frac{\sin[(\varepsilon_{n'}-\varepsilon_0-\hbar\omega)t_{\max}/\hbar]}{(\varepsilon_{n'}-\varepsilon_0-\hbar\omega)/\hbar}.\end{aligned} \tag{30}$$

## III. RESULTS

### A. Potential energy surfaces

The ground state geometry of $CH_2OO$ optimized at the DW-SA-CASSCF level of theory is presented in Fig. 1, along with key geometric parameters at the minimum energy configuration. These parameters are in reasonable agreement with those determined experimentally.[28,29] As outlined in the Introduction, the $R_{O_1O_2}/R_{O_1C}$ ratio has been used extensively in the literature to ascribe a type of electronic character to the Criegee intermediate, i.e., biradical or zwitterionic. Historically, a $R_{O_1O_2}/R_{O_1C}$ value of ~1.10 is indicative of a strong zwitterionic character, whereas $R_{O_1O_2}/R_{O_1C} \sim 1.00$ indicates a biradical character. Recent calculations based on CASSCF[20] and CCSD(T)[17] suggest a predominantly zwitterionic character and reveal $R_{O_1O_2}/R_{O_1C}$ to be ~1.06. At the DW-SA-CASSCF level, $R_{O_1O_2}/R_{O_1C} \sim 1.05$ and a strong dipole moment for the ground state at the equilibrium geometry suggests zwitterionic character. In a separate calculation, we found that the ground state geometry optimized at the level of regular (i.e., non-state averaged) CASSCF with a full valence active space also has a strong dipole moment and a $R_{O_1O_2}/R_{O_1C}$ value of ~1.08. These results indicate that the particular choice of the weighting scheme ($\beta = 2$ eV) leaves the qualitative character of $CH_2OO$ ground state unchanged, even though the quantitative details change, enabling us to compute ground, excited, and interstate properties (e.g., transition dipole moments) from the same calculation.

Potential energy surfaces were constructed around the lowest point on the ground state surface ($E_0 = 188.765$ hartree), found to be at $R_{O_1O_2} = 1.34$ Å and $a_{CO_1O_2} = 120^\circ$. A one-dimensional cut of the adiabatic PESs of $CH_2OO$ along $R_{O_1O_2}$ at $a_{CO_1O_2} = 120^\circ$ is shown in Fig. 2(a). The eight lowest adiabats were found to converge to two different asymptotes separated by 31 kcal mol$^{-1}$ at large $R_{O_1O_2}$. An analysis of the orbital occupations in the dominant configuration state functions indicates that at large O–O distance the lower asymptote leads to the dissociation of $CH_2OO$ into $H_2CO$ ($X\,^1A_1$) and O ($^1D$) fragments, whereas the upper asymptote corresponds to $H_2CO$ ($a\,^3A''$) and O ($^3P$). The energetic separation of these states is close to the experimental value of 26.6 kcal mol$^{-1}$.[56,57]

The most striking feature of the adiabats in Fig. 2(a) is the fact that the surfaces become discontinuous and "rough" as they approach one another. Fig. 2(b) depicts a cut of the diabatic surface at $a_{CO_1O_2} = 120^\circ$, which clearly shows that diabatization has smoothed out the roughness and rendered the surfaces continuous. A series of such one-dimensional cuts of the diabatic surfaces at different $a_{CO_1O_2}$ is given in Fig. 3. These cuts give an overview of the two-dimensional diabatic surfaces used in this work.

The diabatic couplings ($V_{AB}, A \neq B$) are portrayed in Fig. 4. On the one hand, in the region 1.5 Å $< R_{O_1O_2} <$ 1.8 Å with $a_{CO_1O_2} < 120^\circ$, $S_1$ is coupled with $S_3$ and $S_2$ is coupled with $S_4$; in addition for $a_{CO_1O_2} \geq 120^\circ$, $S_1$ is coupled with $S_4$ and $S_2$ is coupled with $S_3$. On the other hand, in the region 2.0 Å $< R_{O_1O_2} <$ 2.5 Å, $S_1$ is coupled with $S_7$ and $S_2$ is

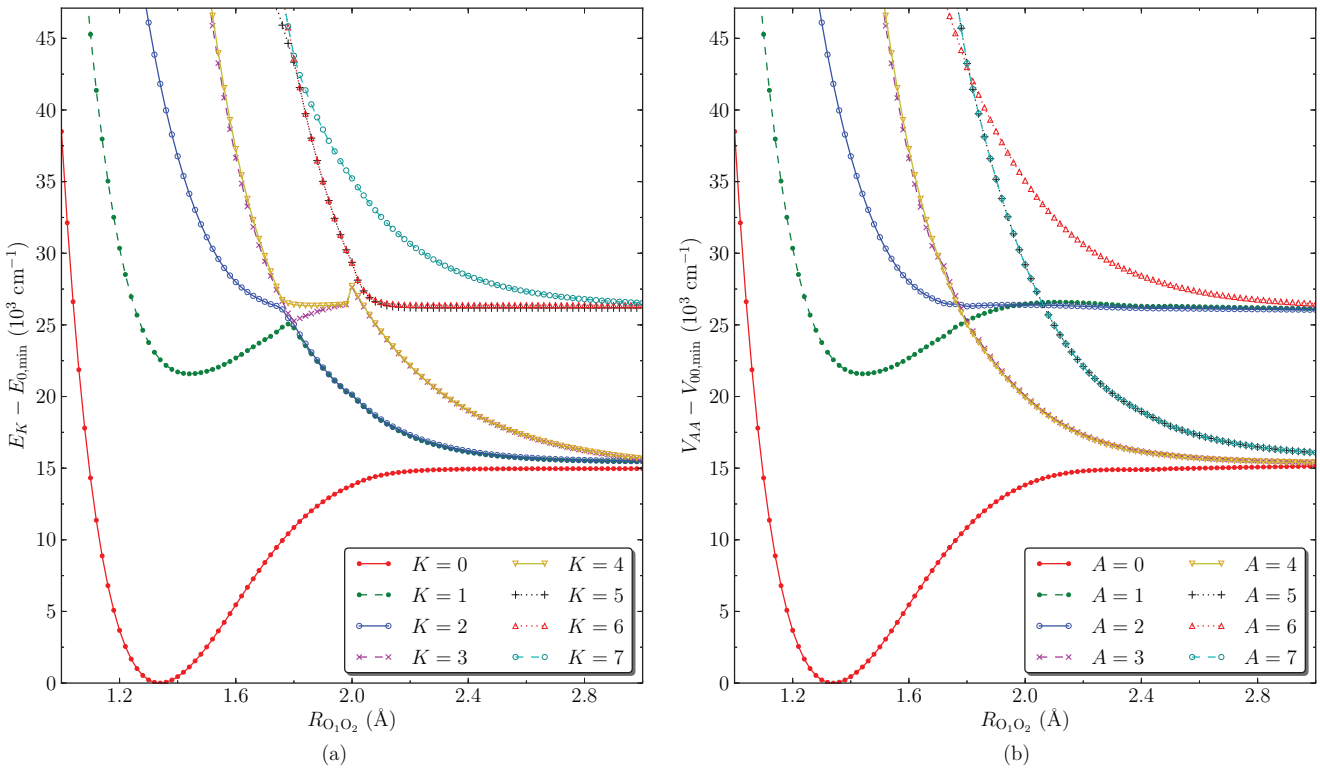


FIG. 2. One-dimensional cuts of the singlet potential energy surfaces in adiabatic (a) and diabatic (b) representations at $a_{CO_1O_2} = 120°$. The lowest point on the ground state surfaces in the two representations is $E_{0,\min} = V_{00,\min} = -188.765$ hartree. The diabatic surfaces $S_3$ and $S_4$ as well as $S_5$ and $S_7$ in panel (b) are overlapping. Similar overlaps can be seen in panel (a) for the corresponding adiabatic surfaces. *K* denotes adiabat state labels, *A* denotes diabatic state labels.

coupled with $S_5$. The relatively higher magnitudes of $V_{23}$ and $V_{24}$ compared to $V_{25}$ indicates higher probability of transfer of population from $S_2$ to the lower dissociation asymptote via $S_3$ and $S_4$, which is important for the dissociation dynamics (see below).

Dipole moments for $S_0$–$S_4$ in the diabatic basis are shown in Fig. 5. For $R_{O_1O_2} > 1.5$ Å, $S_1$, $S_2$, and $S_6$ have small dipole moments indicating low charge separation, whereas $S_3$, $S_4$, $S_5$, and $S_7$ have large dipole moments indicating large charge separation (just as for $S_0$). As such, by design [see Sec. II B], the above diabatic couplings involve coupling between "mostly zwitterionic" states with "mostly biradical" states, respectively. The smoothness of the diabatic surfaces [see Fig. 3] and the small magnitude of the diabatic couplings [see Fig. 4] justify heuristically our construction of the diabatic states according to Sec. II B. Finally, although in this work we cannot rigorously calculate the derivative couplings between our proposed diabats, we are confident such couplings should be small: as Fig. 3 shows, $S_1$ and $S_2$ never cross one another with a large gradient difference, even though they approach the same degenerate limit asymptotically. The same behavior is found for $S_3$ and $S_4$.

### B. Dynamics on the excited state

At $t = 0$, the ground vibronic state $|\Psi_0\rangle$ [see Fig. 6] was excited to $S_2$ and the total wavepacket was propagated on the coupled excited surfaces. As explained in Sec. II D, excitation to $S_2$ is based on the dominant oscillator strength for the $S_2 \leftarrow S_0$ transition [see Table II and Fig. 5(f)] as well as experimental observation[8] of the associated UV absorption spectrum and resultant dissociation dynamics. The $S_6 \leftarrow S_0$ transition also carries significant oscillator strength but the transition frequency ($E_6 - E_0 > 87 \times 10^3$ cm$^{-1}$) is too high to be relevant for previously observed UV spectrum and dynamics.

The movement of the wavepacket is shown in Fig. 7 in terms of the snapshots of $|\xi_2(t)\rangle$, the portion of the wavepacket on $S_2$ [see Eq. (26)]. It is evident that the wavepacket becomes wider as time progresses, and it quickly evolves across the surfaces toward longer $R_{O_1O_2}$ as well as narrower $a_{CO_1O_2}$. The dynamics simulation reveals that only about 4.59% of the excited state population dissociates into $H_2CO$ ($X\,^1A_1$) and O ($^1D$) fragments at the lower dissociation asymptote, while the majority (~95.41%) dissociates into $H_2CO$ ($a\,^3A''$) and O ($^3P$) via the upper asymptote. The transfer of population from $S_2$ to the lower asymptote through $S_3$ (~4.41%), $S_4$ (~0.11%), and $S_5$ (~0.07%) are due to nonzero values of the diabatic couplings in the intersection regions [see Fig. 4].

As a side note, we noticed that if the dynamics of the excited wavepacket is simulated on a one-dimensional slice of the two-dimensional diabatic surfaces at $a_{CO_1O_2} = 120°$, then 4.60% of the population is transferred to the lower asymptote through $S_3$ (~4.55%) and $S_5$ (~0.05%). This agreement indicates that, within our two-dimensional model, the bending motion along $a_{CO_1O_2}$ is not very important in modeling

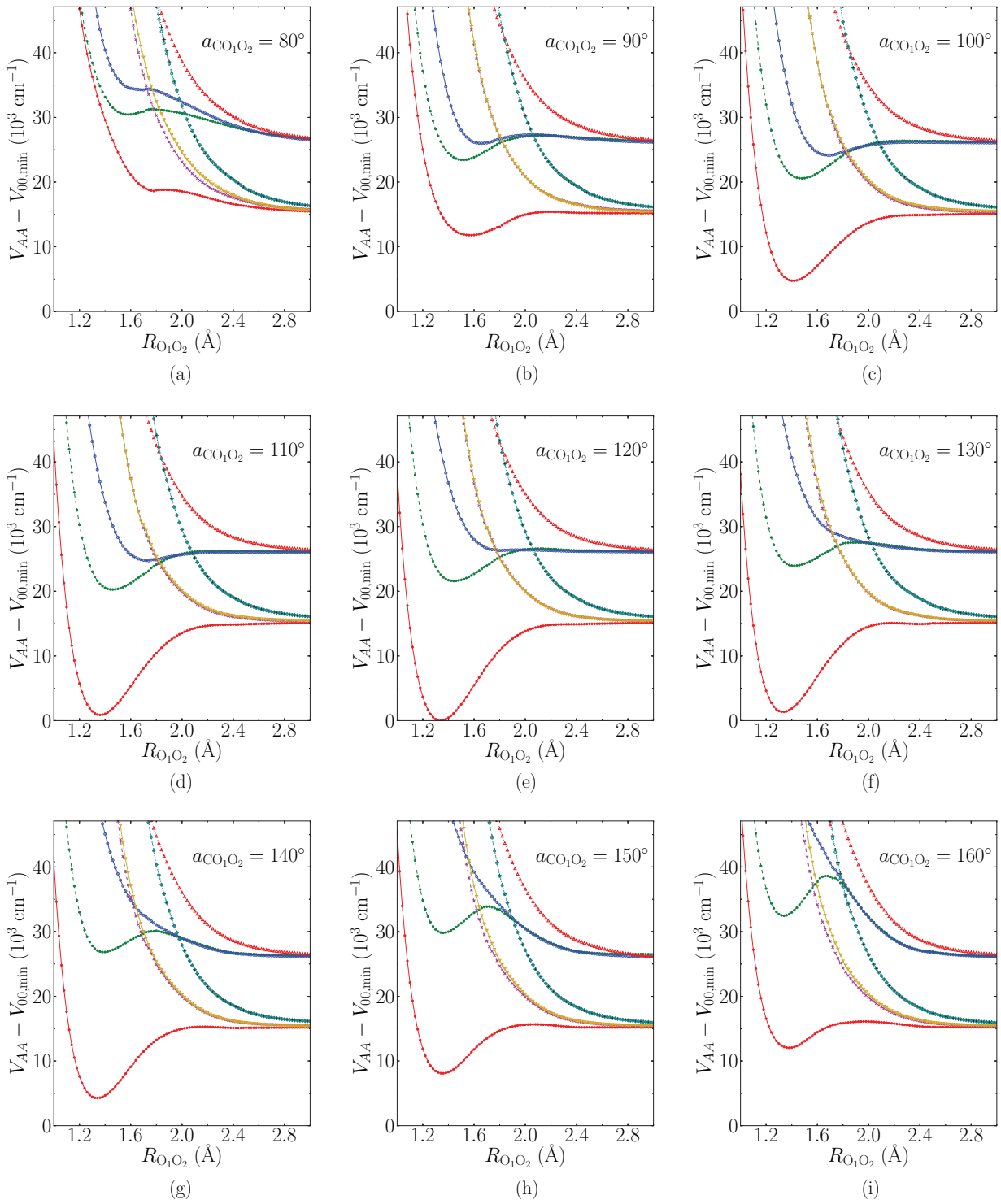


FIG. 3. One-dimensional cuts of the two-dimensional diabatic surfaces ($S_A$) along $R_{O_1O_2}$ at various $a_{CO_1O_2}$ angles from 80° (a) to 160° (i) in 10° increments about the ground state equilibrium angle 120° (e). The legends for all the plots are shown in Fig. 2(b). Potential energy surfaces are shown relative to $V_{00,min} = -188.765$ hartree. *A* denotes diabatic state labels.

the O ($^1D$)/O ($^3P$) branching ratio. However, Fig. 7 clearly illustrates that the wavepacket feels the influence of this coordinate, with the wavepacket evolving to much tighter $a_{CO_1O_2}$ angles toward the dissociation limit.

From the experimental perspective, Lehman *et al.*[11] demonstrated that UV excitation of jet-cooled $CH_2OO$ to the excited *B* state results in prompt dissociation, yielding O ($^1D$) and $H_2CO$ ($X\,^1A_1$) products associated with the lowest spin-allowed channel. Velocity map imaging (VMI) studies of the $CH_2OO$ dissociation dynamics revealed an anisotropic angular distribution, demonstrating that dissociation is rapid compared to $CH_2OO$ rotation (picosecond timescale). The theoretical prediction of the importance of the O ($^3P$) + $H_2CO$ ($a\,^3A''$) channel in the present study has

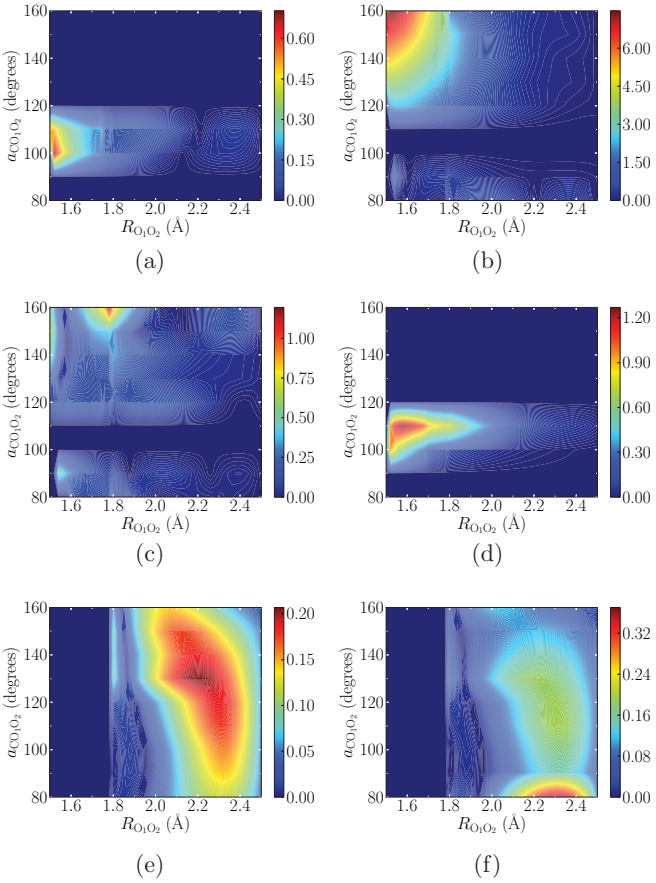


FIG. 4. Two-dimensional plots of the significant diabatic coupling elements in the prompt dissociation of $CH_2OO$ after electronic excitation to the $S_2$ ($B$) state. Values shown are in the units of $10^{-3}$ au. (a) $|V_{13}|$, (b) $|V_{23}|$, (c) $|V_{14}|$, (d) $|V_{24}|$, (e) $|V_{25}|$, (f) $|V_{17}|$.

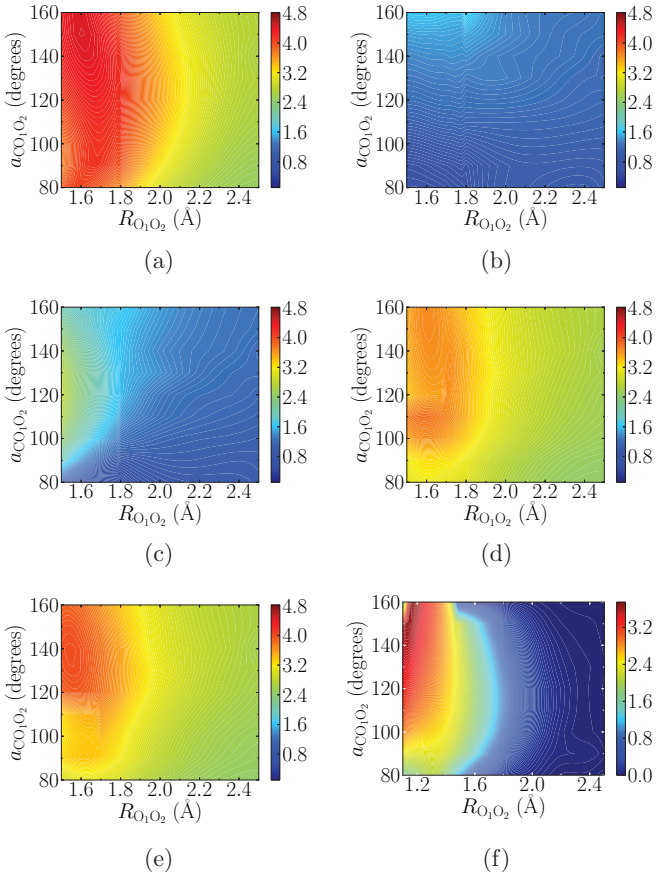


FIG. 5. Norm of the lowest five dipole matrix elements in the diabatic basis for $CH_2OO$. The transition dipole moment $\boldsymbol{\mu}_{02}$ corresponds to the experimentally observed $S_2 \leftarrow S_0$ ($B \leftarrow X$) electronic transition. The smooth nature of these dipole surfaces illustrate the effectiveness of the diabatization method. $S_0$, $S_3$, and $S_4$ exhibit primarily zwitterionic electronic character; $S_1$ and $S_2$ are primarily biradical in nature. (a) $|\mu_{00}|$, (b) $|\mu_{11}|$, (c) $|\mu_{22}|$, (d) $|\mu_{33}|$, (e) $|\mu_{44}|$, (f) $|\mu_{02}|$.

prompted further experimental work. The O ($^3P$) channel has subsequently been observed and characterized using VMI following UV excitation of $CH_2OO$, and will be published in Ref. 12. The branching ratio between O ($^3P$) and O ($^1D$) product channels will be very challenging to determine experimentally, but will be the subject of future work.

### C. Electronic absorption spectra

While the focus of this paper is the photodissociation dynamics of $CH_2OO$, a complete account also includes the related absorption spectrum. The absorption spectrum computed for the $CH_2OO$ $S_2 \leftarrow S_0$ transition is shown in Fig. 8 as a function of photon energy in wavenumbers. The absorption cross section $\sigma(\omega)$ is evaluated according to Eq. (30), scaled to unity at the peak, and labeled as intensity. The 0 K absorption spectrum is computed using the two-dimensional diabatic surfaces along $R_{O_1O_2}$ and $a_{CO_1O_2}$ as well as with one-dimensional cuts along $R_{O_1O_2}$ at $a_{CO_1O_2} = 120°$. The electronic spectra obtained using the 2D and 1D surfaces are almost indistinguishable from one another. Both spectra indicate a maximum absorption near $41 \times 10^3$ cm$^{-1}$, corresponding to ~245 nm, with breadth of $\sim 10 \times 10^3$ cm$^{-1}$.

Also shown in Fig. 8 is the experimental absorption spectrum observed for $CH_2OO$ under jet-cooled conditions. Beames *et al.*[8] showed that $CH_2OO$ has a very strong UV absorption spectrum peaked at 335 nm, corresponding to 30 $\times 10^3$ cm$^{-1}$, with large cross section. The $CH_2OO$ absorption

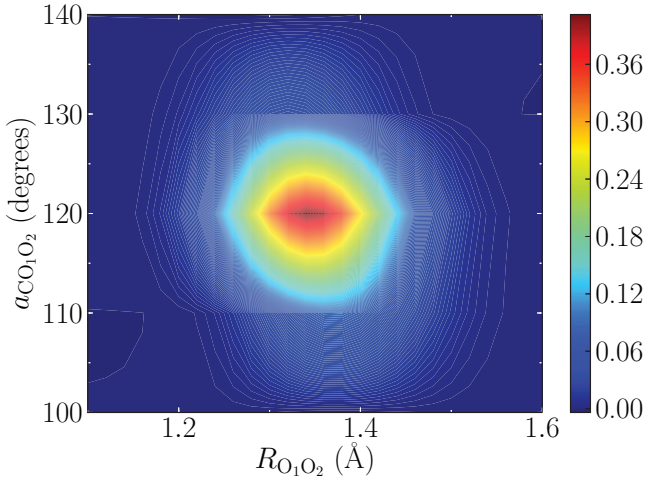


FIG. 6. Two-dimensional plot of the amplitude of the nuclear component of the ground vibronic state wavefunction.

TABLE II. Oscillator strengths ($f_{J0}$) for $S_J \leftarrow S_0$ electronic transitions in the Franck-Condon region ($R_{O_1O_2} = 1.34$ Å, $a_{CO_1O_2} = 120°$) obtained from DW-SA-CASSCF calculations (in terms of adiabats).

| Final state ($J$) | Oscillator strength ($f_{J0}$) |
|---|---|
| 1 | 0.000 |
| 2 | 0.153 |
| 3 | 0.000 |
| 4 | 0.009 |
| 5 | 0.000 |
| 6 | 0.122 |
| 7 | 0.003 |

spectrum was obtained by UV-induced depletion of the VUV photoionization signal at $m/z = 46$. The large UV-induced depletion and broad unstructured spectrum (~40 nm FWHM) are both indicative of rapid dynamics in the $B$ state ($S_2$), consistent with VMI studies showing dissociation on the picosecond timescale.[11] These studies are in accord with a repulsive $B$ state potential along the O–O coordinate computed theoretically in this work and previously.[8,18] We note, however, that the computed absorption spectrum (in Fig. 8) peaks at significantly higher energy and has greater breadth than that observed experimentally. This disagreement is not terribly surprising since the DW-SA-CASSCF method was selected to obtain smooth potential energy surfaces as required for dynamics. A better approach for optical excited state energies would be state specific CASSCF or equally weighted state averaging.

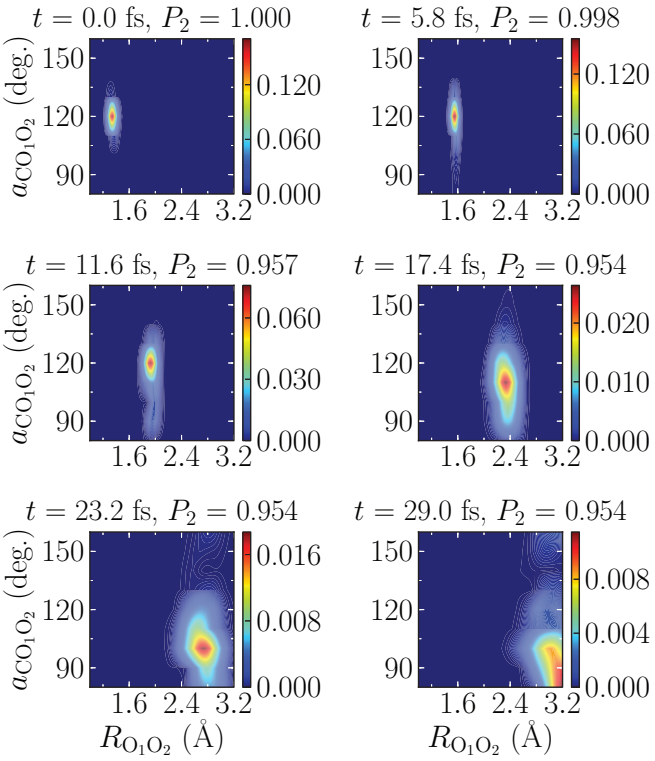


FIG. 7. Snapshots of the wavepacket in motion (on $S_2$) at different times [see Eq. (27)]. The ground state $S_0$ wavefunction is excited to the $S_2$ ($B$) state at t = 0, and evolves to dissociation at the O ($^3P$) and $H_2CO$ ($a\,^3A''$) asymptotic limit within 30 fs.

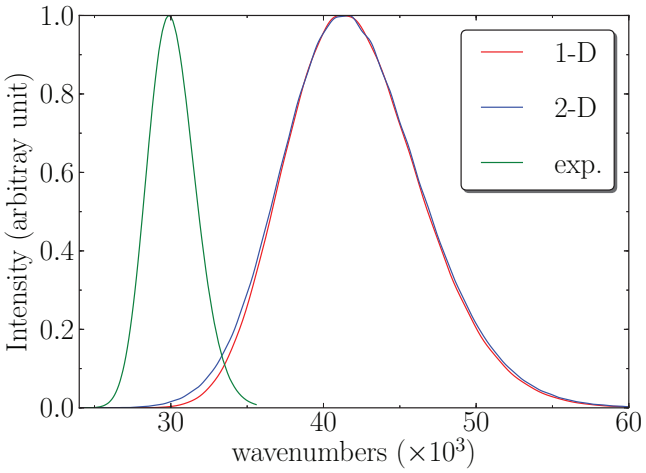


FIG. 8. Electronic absorption spectra for $CH_2OO$ at 0 K. The theoretical spectrum labeled as "1-D" is based on the one-dimensional cut of the diabatic surfaces along $R_{O_1O_2}$ at $a_{CO_1O_2} = 120°$. The spectrum labeled as "2D" is based on the two-dimensional diabatic surfaces. The experimental spectrum is a Gaussian fit to the data. Adapted from Ref. 8. All the spectra were scaled so that the maximum intensity is equal to unity.

To address any concerns regarding accuracy, a separate set of calculations was carried out with different weighting schemes for DW-SA-CASSCF. We found that the choice of a larger $\beta$ (which is equivalent to choosing more similar weights for the $S_0$, $S_1$, and $S_2$ states computed according to Eq. (1)) results in a shift of the absorption maximum toward lower energy as well as a reduction in its breadth. For example, the absorption spectrum determined with $\beta = 6$ eV shows a peak near $34 \times 10^3$ cm$^{-1}$ and a breadth of about $7 \times 10^3$ cm$^{-1}$, in closer accord with experiment. As $\beta$ is increased, the energy gap between the ground $S_0$ and the excited $S_2$ states decreases, and the $S_2$ surface becomes less steep in the Franck-Condon region, giving rise to the spectral shift and narrower breadth of the absorption spectrum, respectively. Assuming that the calculated potential energy surfaces ($\beta = 2$) overestimate the slope of the repulsive wall, this would also result in a shortened timescale for dissociation.

Unfortunately, DW-SA-CASSCF with larger $\beta$ tends to generate adiabatic surfaces that are very rugged even at geometries away from the relevant low-lying crossing regions. This is a common problem for regular state-averaged CASSCF where all the computed states are weighted equally. We also found that these rough spots could not be remedied by diabatizing just the seven lowest singlet excited states. Thus for now we have settled on calculations with $\beta = 2$ eV as a good compromise between smooth surfaces for dynamics and absolute excitation energies. Future work will no doubt sample larger active spaces and ideally achieve state averaging CASSCF without dynamical weighting for improved accuracy.

## IV. CONCLUSIONS

We have presented a theoretical investigation of the electronic spectroscopy and excited state dynamics of the

simplest Criegee intermediate $CH_2OO$. The first eight singlet adiabatic states were computed on a two-dimensional grid along the O–O bond length and C–O–O bond angle using a dynamically weighted state-averaged CASSCF method. Several of the low-lying singlet states come in close proximity to one other, leading to discontinuities in the adiabatic surfaces. As a result, quasi-diabatic states and diabatic couplings were obtained by maximizing the charge separation between the states, and used to generate smooth surfaces for simulating the dissociation dynamics and estimating the absorption spectrum.

Our overall conclusions are as follows: after electronic excitation of $CH_2OO$ to the excited $S_2$ ($B$) state, the vast majority of population (~95%) remains on the $S_2$ state to large O–O distance and rapidly dissociates into $H_2CO$ ($a\,^3A''$) and O ($^3P$) fragments. The balance (~5%) is transferred to the lowest spin allowed asymptote due to coupling with other diabatic states, resulting in $H_2CO$ ($X\,^1A_1$) and O ($^1D$) fragments. The O ($^1D$) product channel has been observed experimentally,[11] and the predicted significance of the O ($^3P$) channel has prompted new experiments which will be presented in Ref. 12. Our computed absorption spectrum for $CH_2OO$ at 0 K is quite broad and structureless, lacking any vibrational features, due to the dissociative nature of the excited $S_2$ electronic state. This featureless spectrum is consistent with the experimental absorption spectrum recorded by Beames *et al.*[8] at 10 K, but not with the experimental reports by Sheps[9] and Ting *et al.*[10] showing diffuse structure on the long wavelength tail at 300 K. Future research may benefit from using a higher level electronic structure theory method that could utilize a larger active space and better account for any dynamic electron correlation effects (e.g., multi-reference configuration interaction calculations (MRCI)[58]) as well as exploring more nuclear motions, ideally all nine degrees of freedom.

## ACKNOWLEDGMENTS

This research was supported, in part, by the National Science Foundation CAREER Grant No. CHE-1150851 (J.E.S.) and the U.S. Department of Energy, Basic Energy Sciences (Grant No. DE-FG02-87ER13792) (M.I.L.). J.M.B. acknowledges support through the Dreyfus Postdoctoral Program in Environmental Chemistry (Grant No. EP-12-025). K.S. would like to thank Dr. Andrew Petit for his help in the construction of the nuclear kinetic energy matrix in terms of internal coordinates using the discrete variable representation approach.

[1]R. Criegee, Angew. Chem., Int. Ed. **14**, 745 (1975).
[2]S. D. Piccot, J. J. Watson, and J. W. Jones, J. Geophys. Res., [Atmos.] **97**, 9897, doi:10.1029/92JD00682 (1992).
[3]A. Guenther, C. N. Hewitt, D. Erickson, R. Fall, C. Geron, T. Graedel, P. Harley, L. Klinger, M. Lerdau, W. A. McKay, T. Pierce, B. Scholes, R. Steinbrecher, R. Tallamraju, J. Taylor, and P. Zimmerman, J. Geophys. Res., [Atmos.] **100**, 8873, doi:10.1029/94JD02950 (1995).
[4]D. Johnson and G. Marston, Chem. Soc. Rev. **37**, 699 (2008).
[5]N. M. Donahue, G. T. Drozd, S. A. Epstein, A. A. Presto, and J. H. Kroll, Phys. Chem. Chem. Phys. **13**, 10848 (2011).
[6]O. Welz, J. D. Savee, D. L. Osborn, S. S. Vasu, C. J. Percival, D. E. Shallcross, and C. A. Taatjes, Science **335**, 204 (2012).
[7]C. A. Taatjes, O. Welz, A. J. Eskola, J. D. Savee, D. L. Osborn, E. P. F. Lee, J. M. Dyke, D. W. K. Mok, D. E. Shallcross, and C. J. Percival, Phys. Chem. Chem. Phys. **14**, 10391 (2012).
[8]J. M. Beames, F. Liu, L. Lu, and M. I. Lester, J. Am. Chem. Soc. **134**, 20045 (2012).
[9]L. Sheps, J. Phys. Chem. Lett. **4**, 4201 (2013).
[10]W.-L. Ting, Y.-H. Chen, W. Chao, M. C. Smith, and J. J.-M. Lin, Phys. Chem. Chem. Phys. **16**, 10438 (2014).
[11]J. Lehman, H. Li, J. M. Beames, and M. I. Lester, J. Chem. Phys. **139**, 141103 (2013).
[12]H. Li, Y. Fang, J. M. Beames, and M. I. Lester, personal communication (2014).
[13]A. Kalemos and A. Mavridis, J. Chem. Phys. **129**, 054312 (2008).
[14]P. J. Hay, T. H. Dunning, and W. A. Goddard, J. Chem. Phys. **62**, 3912 (1975).
[15]W. R. Wadt and W. A. Goddard, J. Am. Chem. Soc. **97**, 3004 (1975).
[16]R. Gutbrod, R. N. Schindler, E. Kraka, and D. Cremer, Chem. Phys. Lett. **252**, 221 (1996).
[17]D. Cremer, J. Gauss, E. Kraka, J. F. Stanton, and R. J. Bartlett, Chem. Phys. Lett. **209**, 547 (1993).
[18]P. Aplincourt, E. Henon, F. Bohr, and M. F. Ruiz-Lopez, Chem. Phys. **285**, 221 (2002).
[19]D.-C. Fang and X.-Y. Fu, J. Phys. Chem. A **106**, 2988 (2002).
[20]M. T. Nguyen, T. L. Nguyen, V. T. Ngan, and H. M. T. Nguyen, Chem. Phys. Lett. **448**, 183 (2007).
[21]J. M. Hermida-Ramón, A. Öhrn, and G. Karlström, Chem. Phys. **359**, 118 (2009).
[22]E. Miliordos, K. Ruedenberg, and S. S. Xantheas, Angew. Chem., Int. Ed. **52**, 5736 (2013).
[23]J. Kalinowski, M. Rsnen, P. Heinonen, I. Kilpelinen, and R. B. Gerber, Angew. Chem., Int. Ed. **53**, 265 (2014).
[24]W. Sander, Angew. Chem., Int. Ed. **29**, 344 (1990).
[25]J. M. Anglada, J. Gonzalez, and M. Torrent-Sucarrat, Phys. Chem. Chem. Phys. **13**, 13034 (2011).
[26]J. Li, S. Carter, J. M. Bowman, R. Dawes, D. Xie, and H. Guo, J. Phys. Chem. Lett. **5**, 2364 (2014).
[27]E. P. F. Lee, D. K. W. Mok, D. E. Shallcross, C. J. Percival, D. L. Osborn, C. A. Taatjes, and J. M. Dyke, Chem. Eur. J. **18**, 12411 (2012).
[28]M. Nakajima and Y. Endo, J. Chem. Phys. **139**, 101103 (2013).
[29]M. C. McCarthy, L. Cheng, K. N. Crabtree, O. Martinez, T. L. Nguyen, C. C. Womack, and J. F. Stanton, J. Phys. Chem. Lett. **4**, 4133 (2013).
[30]Y.-T. Su, Y.-H. Huang, H. A. Witek, and Y.-P. Lee, Science **340**, 174 (2013).
[31]W. W. Sander, J. Org. Chem. **54**, 333 (1989).
[32]J. M. Beames, F. Liu, L. Lu, and M. I. Lester, J. Chem. Phys. **138**, 244307 (2013).
[33]M. P. Deskevich, D. J. Nesbitt, and H. Werner, J. Chem. Phys. **120**, 7281 (2004).
[34]R. N. Diffenderfer and D. R. Yarkony, J. Phys. Chem. **86**, 5098 (1982).
[35]M. Schmidt, K. Baldridge, J. Boatz, S. Elbert, M. Gordon, J. Jensen, S. Koseki, N. Matsunaga, K. Nguyen, S. Su, T. Windus, M. Dupuis, and J. Montgomery, J. Comput. Chem. **14**, 1347 (1993).
[36]M. S. Gordon and M. W. Schmidt, in *Theory and Applications of Computational Chemistry: The First Forty Years*, edited by C. Dykstra, G. Frenking, K. Kim, and G. Scuseria (Elsevier, Amsterdam, 2005).
[37]T. H. Dunning, Jr., J. Chem. Phys. **90**, 1007 (1989).
[38]T. H. Dunning, Jr. and P. J. Hay, in *Methods of Electronic Structure Theory*, edited by H. F. Schaeffer III (Plenum Press, 1977), Vol. 2.
[39]Data points between $R_{O_1O_2} = 2.5$ and $R_{O_1O_2} = 2.98$ were sometimes difficult to converge. Because these geometries are located far from crossing regions, the energies were safely interpolated using cubic splines.
[40]F. T. Smith, Phys. Rev. **179**, 111 (1969).
[41]C. A. Mead and D. G. Truhlar, J. Chem. Phys. **77**, 6090 (1982).
[42]H. Köppel, in *Conical Intersections: Electronic Structure, Dynamics and Spectroscopy*, edited by W. Domcke, D. R. Yarkony, and H. Köppel (World Scientific, New Jersey, 2004), p. 175.
[43]R. J. Cave and M. D. Newton, Chem. Phys. Lett. **249**, 15 (1996).
[44]R. J. Cave and M. D. Newton, J. Chem. Phys. **106**, 9213 (1997).
[45]J. E. Subotnik, S. Yeganeh, R. J. Cave, and M. A. Ratner, J. Chem. Phys. **129**, 244101 (2008).
[46]J. E. Subotnik, R. J. Cave, R. P. Steele, and N. Shenvi, J. Chem. Phys. **130**, 234102 (2009).

[47]E. Alguire and J. E. Subotnik, J. Chem. Phys. **135**, 044114 (2011).
[48]S. Fatehi, E. Alguire, and J. E. Subotnik, J. Chem. Phys. **139**, 124112 (2013).
[49]C. Edmiston and K. Ruedenberg, Rev. Mod. Phys. **35**, 457 (1963).
[50]D. R. Yarkony, J. Phys. Chem. A **102**, 8073 (1998).
[51]M. Born and K. Huang, *Dynamical Theory of Crystal Lattices* (Oxford University Press, Oxford, 1954).
[52]To emphasize that $\{|\Xi_A\rangle\}$ are quasi-diabatic, we shall drop the weak dependence on **R** from now on.
[53]J. H. Frederick and C. Woywod, J. Chem. Phys. **111**, 7255 (1999).
[54]A. S. Petit and A. B. McCoy, J. Phys. Chem. A **117**, 7009 (2013).
[55]E. J. Heller, Acc. Chem. Res. **14**, 368 (1981).
[56]G. Herzberg, *Molecular Spectra and Molecular Structure: 3. Electronic Spectra and Electronic Structure of Polyatomic Molecules*, 2nd ed. (Van Nostrand, New York, 1950).
[57]C. E. Moore, in *CRC Series in Evaluated Data in Atomic Physics*, edited by J. W. Gallagher (CRC Press, Boca Raton, FL, 1993), p. 339.
[58]R. Dawes, personal communication (2014).